



Mixed anodic oxides for forming-free memristors revealed by combinatorial screening of hafnium-tantalum system

Ivana Zrinski^a, Alexey Minenkov^b, Claudia Cancellieri^c, Roland Hauert^c,
Cezarina Cela Mardare^{a,d}, Jan Philipp Kollender^c, Lars P.H. Jeurgens^c, Heiko Groiss^b,
Achim Walter Hassel^{a,d}, Andrei Ionut Mardare^{a,*}

^a Institute of Chemical Technology of Inorganic Materials, Johannes Kepler University Linz, Altenberger Str. 69, Linz 4040, Austria

^b Christian Doppler Laboratory for Nanoscale Phase Transformations, Center for Surface and Nanoanalytics, Johannes Kepler University Linz, Altenberger Str. 69, Linz 4040, Austria

^c EMPA, Laboratory for Joining Technologies and Corrosion, Swiss Federal Laboratories for Materials Science and Technology, Überlandstrasse 129, Dübendorf 8600, Switzerland

^d Danube Private University, Steiner Landstrasse 124, Krems-Stein 3500, Austria

ARTICLE INFO

Article history:

Received 22 July 2021

Revised 27 September 2021

Accepted 8 November 2021

Keywords:

Metallic thin films
Combinatorial libraries
Anodic memristors
Anodic oxides
Valve metals

ABSTRACT

A combinatorial screening approach has been designed for identification of Hf-Ta anodic memristors with enhanced properties. Three distinct compositional zones with similar characteristics have been identified, two of which are relevant for memristive applications. In a Hf-poor zone, (< 50 at.% Hf), the memristive behavior is similar to that of anodic Ta₂O₅. A second compositional zone (Hf content between 50 and 70 at.%) produced anodic memristors which dramatically differ. Devices in this region resemble forming-free unipolar behavior and show resistive states ratios of more than 8 orders of magnitude while retaining and enduring more than one million switching cycles. Photoelectron spectroscopy with soft and hard X-rays has been applied for understanding the chemistry of these special anodic structures and enrichment of Hf species close to the surface of anodic oxides has been evidenced. Unlike bipolar memristors from the first zone, the newly identified unipolar memristors show an in-depth homogeneous local chemical state of Hf and lower electronic polarizabilities for both O and Hf. High-resolution transmission electron microscopy reveals HfO₂ crystallites embedded into an amorphous oxide matrix. These entities formed during the anodization process are considered to be responsible for the coexistence of threshold and non-volatile memristive characteristics.

© 2021 The Author(s). Published by Elsevier Ltd.

This is an open access article under the CC BY license (<http://creativecommons.org/licenses/by/4.0/>)

1. Introduction

In the field of redox-based resistively switching random access memories (ReRAMs) [1], a great scientific interest has been drawn to the appearance of memristive devices. Memristors [2,3]

Abbreviations: random access memories, (ReRAMs); complementary metal-oxide-semiconductor, (CMOS); conductive filaments, (CF); high resistance state, (HRS); low resistance state, (LRS); metal-insulator-metal, (MIM); valence change memory, (VCM); electrochemical metallization memory, (ECM); energy-dispersive x-ray spectroscopy, (EDX); scanning edx, (SEDx); standard hydrogen electrode, (SHE); citrate buffer, (CB); scanning electron microscopy, (SEM); pulsed voltage stress, (PVS); high-resolution transmission electron microscopy, (HRTEM); focused ion beam, (FIB); X-ray photoelectron spectroscopy, (XPS); hard X-ray photoelectron spectroscopy, (HAXPES); inelastic mean free path, (IMFP); phosphate buffer, (PB); Auger parameter, (AP); fast Fourier transform, (FFT); nanoparticles, (NPs).

* Corresponding author.

E-mail address: andrei.mardare@jku.at (A.I. Mardare).

have shown remarkable electronic and memory characteristics required for data processing [4,5]. Such devices are necessary to overcome the inherent limitations of complementary metal-oxide-semiconductor-based (CMOS) computing architectures [6] via their employment in hardware as bioinspired neural networks [7,8]. Beside, their advantages such as high power efficiency, high reliability and fast operational speed are opportune for use in various data storage devices [9] and logic circuits [10].

Memristors are structured as an oxide layer sandwiched between two metallic electrodes [11,12]. Recently, valve metals and their oxides [13–15], particularly oxidized Hf and Ta, have been studied for memristive applications [16–19] since they have been identified as promising candidates for capacitors, metal-oxide-semiconductor transistors and high power resistors [20,21]. Both HfO₂ and Ta₂O₅ are already listed as high dielectric constant materials [17] and their attractive properties such as high thermal and chemical stability, sustained low leakage current values and high

breakdown field strength can be further improved by alloying both materials [22]. Metastable and amorphous phases of Hf-Ta systems have been produced by co-deposition techniques onto low-temperature substrates, directly influencing the final properties of their mixed anodic oxides [22]. Additionally, the different anodic growth dynamics of Hf and Ta oxides, influenced by very different ionic transport numbers, may induce formation of numerous accumulation regions at certain positions inside the oxide layer [23]. In turn, this may lead to spatial pinning of conductive filaments (CF), which are responsible for the switching between the high resistance state (HRS) and the low resistance state (LRS) of a memristive device. According to literature, the CFs formation [24] in memristors, within a metal-insulator-metal (MIM) structure, is based on the valence change memory (VCM) or the electrochemical metalization memory (ECM) formation mechanisms [6]. In general, the solid electrolyte is partially reduced, forming positively charged local oxygen-deficient regions, which are compensated by electrons from the redox reactions, consequently [6,9].

The aim of the current work is to achieve a compositionally controlled CF formation process in mixed Hf-Ta anodic oxides and to explore the feasibility of forming-free Hf-Ta/HfO₂-Ta₂O₅/Pt memristors. This is done by screening a Hf-Ta thin film combinatorial library with a broad compositional range. Previous studies of Ta- and Hf-based memristors [25,26] have shown that the simple and inexpensive process of anodization led to the fabrication of high-quality memristive systems [18,27,28]. Hence, anodization is used here as a convenient method for the production of enduring, stable and reliable memristors. The combinatorial library screening approach allows specifying alloy compositions, which are optimal for the memristive capabilities enhancement of the devices (the HRS/LRS ratio and retention time) and, additionally, brings more light to the reversibility of CFs.

2. Experimental section

2.1. Fabrication of Hf-Ta thin film library

The Hf-Ta thin film combinatorial library was deposited by co-sputtering on Si substrates employing an ultra-high vacuum system (Mantis Deposition, United Kingdom). The substrates were previously thermally oxidized in air at 950 °C for 24 h. The process was done in DC mode using Hf and Ta high purity targets (99.95% Demaco, The Netherlands) and the base pressure of the vacuum system was in the range of 10^{-6} Pa. The Hf and Ta targets were arranged at opposite edges of the substrates for maximizing the compositional spread. The target - substrates distance was set to 13 cm. The deposition was carried out at room temperature, in Ar atmosphere with a pressure of 5×10^{-1} Pa. To screen the entire library, three Si wafers each having a different compositional spread were sequentially used as substrates in a row of independent depositions. In order to tune the Hf-Ta gradients, the powers applied to the Hf and Ta sputtering targets were varied for each deposition between 25 W and 80 W, depending on the desired compositional range. At the center of the Si wafer, the thickness of the film was approximately 300 nm. Pure Hf and Ta films were additionally deposited in identical conditions serving as reference samples during property mapping of the Hf-Ta library. More details about the fabrication of the reference samples can be found elsewhere [18,27,28]. Immediately after deposition, without breaking the vacuum, each wafer from the library was transported into a scanning energy-dispersive X-ray spectroscopy (SEDX) system attached to the same vacuum chamber cluster. This self-developed system for thin film analysis uses a 20 keV electron beam with a spot size of 500 μ m. More experimental details can be found elsewhere [29]. Using the SEDX, the compositional gradient along

the Hf-Ta library was quantified. The resolution of compositional screening was ± 0.5 at.%.

2.2. Fabrication of Hf-Ta anodic memristor library

The Hf-Ta thin film library served as a bottom electrode in a metal-insulator-metal (MIM) structure developed further. The insulating layer was fabricated by electrochemical anodization of the Hf-Ta alloys in a classical three-electrode electrochemical cell. The system consisted of the Si substrates coated with the Hf-Ta library as working electrodes, Hg/Hg₂SO₄/sat. K₂SO₄ electrode (0 V vs. Hg/Hg₂SO₄ = 0.640 V vs. SHE) as reference electrode and a graphite foil (0.5 mm thick, 99.8% Thermo Fisher, Germany) as counter electrode. Cyclic voltammetry was performed with a CompactStat potentiostat (Ivium Technologies, The Netherlands) from 0 V up to 8 V (vs. SHE) at a scan rate of 100 mV s⁻¹. Potentiodynamic growth of anodic oxides was done in ambient conditions in a 0.1 M citrate buffer (CB), pH 6.0, prepared by following the standard procedure for this electrolyte [30]. The choice of specified potentiodynamic growth parameters together with specifics of the electrolyte buffer has been motivated by recent findings in the field [27,28]. All the chemicals citric acid monohydrate (C₆H₈O₇, 5949-29-1) and trisodium citrate dihydrate (C₆H₉Na₃O₇, 6132-04-3) were of analytical grade and were used as received (Merck, Germany). The samples were cleaned and solutions were prepared with ultrapure water (Arium mini, Sartorius, 18 M Ω cm). Finally, approximately 100 nm thick Pt top electrodes were sputtered on top of the anodized Hf-Ta library in Ar atmosphere (5×10^{-1} Pa) at room temperature. The substrates were rotated with 5 rpm in order to obtain Pt thin film uniformity. The patterning of round Pt electrodes, 200 μ m in diameter, was performed using a 30 μ m thick Ni shadow mask foil (Mecachimique, France) pre-attached in intimate contact with the anodized surface. Approximately 300 electrode clusters (5×5 within 3×3 mm² surface area) were patterned on each of the three wafers defining the anodic memristor library.

2.3. Electrical characterization

The electrical measurements performed for characterizing the memristive behavior along the Hf-Ta anodic memristor library are classified into three groups: (1) *I-U* sweeps, (2) endurance and (3) retention tests. All tests were performed in a scanning manner in ambient conditions (22 °C, 55% RH) by an experimental setup specifically designed for this purpose. The setup contains a self-developed Gantry robot with high precision XYZ translation stages, two microscopes cameras (Bresser, Germany) for top- (90°) and side- (45°) views of the Pt top electrodes. A W needle (10 μ m tip diameter) was attached to the Z-stage in order to sequentially electrically connect each addressed top electrode. The contact force is adjusted by feedback to a force sensor and was kept at 20 ± 2 mN. The bottom electrodes (Hf-Ta thin film library) were contacted by an additional contacting needle positioned at the edge of the wafers. The measurements were conducted by a source meter (Keithley 2450) controlled by a LabView® software (self-developed). During all types of measurements (*I-U* sweeps, retention and endurance tests), the Pt top electrode remained grounded, whereas the voltage bias was applied to the Hf-Ta bottom electrode. The voltage never exceeded more than ± 4.0 V (*U*_{set} and *U*_{reset}) and current compliances of 100 mA maximum were applied. Endurance tests were performed by using the pulsed voltage stress (PVS) method at a maximum of 260 Hz, which is the upper limit of the Keithley instrument used. The current limitations utilized for retention and endurance measurements were set up to 20 mA for bipolar and 50 mA for unipolar devices. The resistance of the

memristors, relevant for endurance and retention studies, was obtained by reading the current corresponding to 0.02 V polarization voltage.

2.4. Microscopic and spectroscopic analysis

The electrodes patterning and surface morphology were preliminarily investigated in a plan-view geometry via field emission scanning electron microscopy (SEM). A CrossBeam 1540 XB microscope (ZEISS, Germany) operated at 20 kV accelerating voltage was employed and a secondary electrons detector was used for image acquisition. High-resolution transmission electron microscopy (HRTEM) investigation was performed on memristors using a JEM-2200FS (JEOL, Japan) fitted with in-column Ω -filter, a TemCam-XF416 (TVIPS, Germany) CMOS-based camera and operated at an acceleration voltage of 200 kV. Snaps were recorded applying zero-loss filtering. Gatan DigitalMicrographTM software was used for HRTEM image processing. Thin TEM lamellas were prepared in cross-sectional geometry utilizing focused ion beam (FIB) milling (CrossBeam 1540-XB). The FIB was operated at an acceleration voltage of 30 kV for sample cutting and lift-out and at 5 kV for final thinning. Energy-dispersive X-ray spectroscopy (EDX) analysis was performed in scanning (S)TEM mode for qualitative elemental characterization of specimens. For this purpose, the microscope is equipped with an EDX detector from Oxford Instruments (UK). Elemental maps were constructed and analyzed with Aztec software (v.4.1).

The chemical composition of anodic memristors grown in different electrolytes was evaluated by X-ray photoelectron spectroscopy (XPS) and hard X-ray photoelectron spectroscopy (HAXPES). Analysis using HAXPES and XPS was performed with a PHI Quantes spectrometer (ULVAC-PHI) equipped with a conventional low-energy Al-K α X-ray source (1486.6 eV) and a high energy Cr-K α (5414.7 eV) X-ray source. Both sources are high flux focused monochromatic X-ray beams that can be scanned across the sample surface selected area. The energy scale of the hemispherical analyzer was calibrated according to ISO 15472 by referencing the Au 4f7/2 and Cu 2p3/2 main peaks (as measured *in situ* for corresponding sputter-cleaned, high-purity metal references) to the recommended binding energy (BE) positions of 83.96 eV and 932.62 eV, respectively. Charge neutralization during each measurement cycle was accomplished by a dual beam charge neutralization system, employing low energy electron and Ar ion beams (1 V Bias, 20 μ A current). The core level measurements with both sources were performed in high-power mode. The electron beam is scanned to deconcentrate heat dissipation; hence the analysis is performed along a line 1400 μ m long. The step size and pass energy for core level measurements were 0.2 eV and 112 eV, respectively, for both sources (surveys were acquired at 280 eV pass energy and 0.5 eV step). The atomic concentrations were calculated from the peak areas after Shirley background subtraction using the predefined sensitivity factors in the MultiPak 9.9 software provided by ULVAC-PHI. Compositional depth profiles were recorded by employing alternating cycles of XPS analysis (Al-K α at 51 W; beam diameter \sim 200 μ m) and sputtering with a focused 1 keV Ar beam, rastering an area of 2×2 mm². During each measurement cycle, the Ta 4f, Hf 4f, C 1 s, and O 1 s regions were recorded with a step size of 0.05 eV and a pass energy of 55 eV. The etch rate was determined to be 2.3 nm min⁻¹ on a 100 nm thick Ta₂O₅/Ta reference/calibration sample (Physical Electronics).

To reconstruct the distribution of the different species as a function of depth, the StrataPHI V1.3 simulation program, provided by Physical Electronics USA Inc. was used. This application simulates the layer thicknesses and composition for thin-film structures composed of discrete layers. For each XPS peak measured and for each material the escaping electron was subjected to the Tanuma

Powell and Penn algorithm (TPP-2 M) [31] to calculate its inelastic mean free path (IMFP). This calculation requires the density, atomic weight, band gap and the number of valence electrons of each compound involved. Thereafter, from the measured intensity of the Ta 4f, Hf 4d and O 1 s HAXPES signals, the application calculates the relative contribution of each compound in each layer, as well as the layer thickness for a given layered system.

2.5. Combinatorial screening strategies

Particularities of the Hf-Ta anodic memristor library formation are presented step-wise in Fig. 1. The first step schematically describes the principle of Hf and Ta co-sputtering (in vacuum, without substrate rotation), having as a result a Hf-Ta compositional spread on the substrate. Thus, a high number of Hf-Ta alloys are produced at the same time and under identical conditions, which allows compositional screening of different variables as further discussed. It should be noted that the alloys singled out from such screening can be easily reproduced on the entire surface of fresh substrates, by adjusting the sputtering power of each source and by rotating the substrate during deposition. The second step involves anodization of the entire available surface of the Hf-Ta thin film library (up to 8 V for 20–30 nm thick oxides formed in CB) in a very straightforward manner by dipping the samples into the electrolyte. As soon as the anodic oxide forms on the surface, a mixture of HfO₂ and Ta₂O₅ is expected and controlled by the composition of the parent metallic alloys [22]. Analysis of this mixture's memristive performance is the major goal of the present study and will be presented further for a high number of Hf-Ta alloys.

Finally, the anodized Hf-Ta library is transformed into an anodic memristor library in the next step by patterning Pt top electrodes (see Fig. 1), thus finalizing the fabrication of the MIM structure necessary for electrical investigations. Also, a schematic description of the electrical scanning principle related to further memristive investigations is presented in Fig. 1 as the last experimental step. This may be the most important step since its proper implementation is responsible for the entire amount of data generated during the library scan (which in the present study was computer-assisted) and presents the basis for further analysis and interpretation. Memristive switching capabilities of Hf-Ta anodic oxides were screened along the entire compositional spread. First, forming voltages were identified for each composition along the entire library, then *I*-*U* curves were recorded for each memristor for analyzing its switching behavior.

Electrolyte selection for anodization of the Hf-Ta thin film library was performed based on preliminary results on memristors grown on pure Hf and Ta films (deposited in identical conditions as the Hf-Ta library). Previous studies of Hf anodic memristors confirmed incorporation of electrolyte species in the oxide film [18,28]. When anodizing pure Ta films in phosphate buffer (PB), approximately 5 at.% P was found inside the anodic oxide and no incorporation of C from CB was observed [27], whereas anodization of pure Hf resulted in incorporation of 8 at.% C from CB [28]. In both cases, the electrical properties were affected by this incorporation. On one hand, the incorporation of P improved memristive performance regarding their stability and lifetime in the case of devices based on Ta. On the other hand, the incorporation of P negatively affected device performance regarding lifetime and stability in the case of Hf devices. However, the anodization of pure Ta films in PB and CB produced equally successful memristive devices. Since the best performance of Hf-based memristors was achieved when anodizing in CB, this buffer was chosen for Hf-Ta library anodization in the present work. Additionally, the electrical properties of the best memristors based on pure metals have been used as references for screening of the Hf-Ta library [27,28].

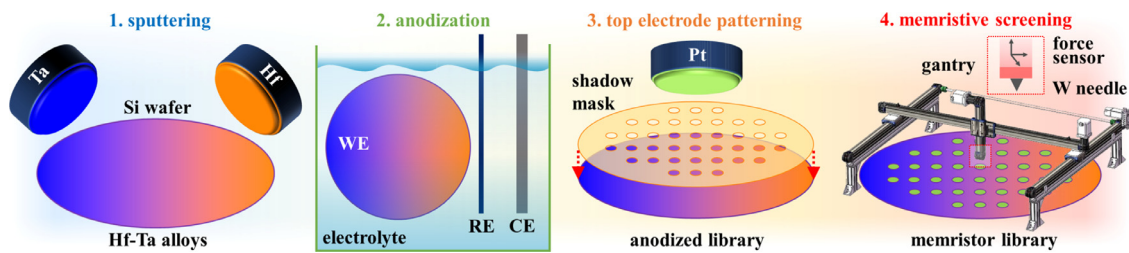


Fig. 1. Schematic representation of experimental steps for fabrication and screening of anodic Hf-Ta memristors.

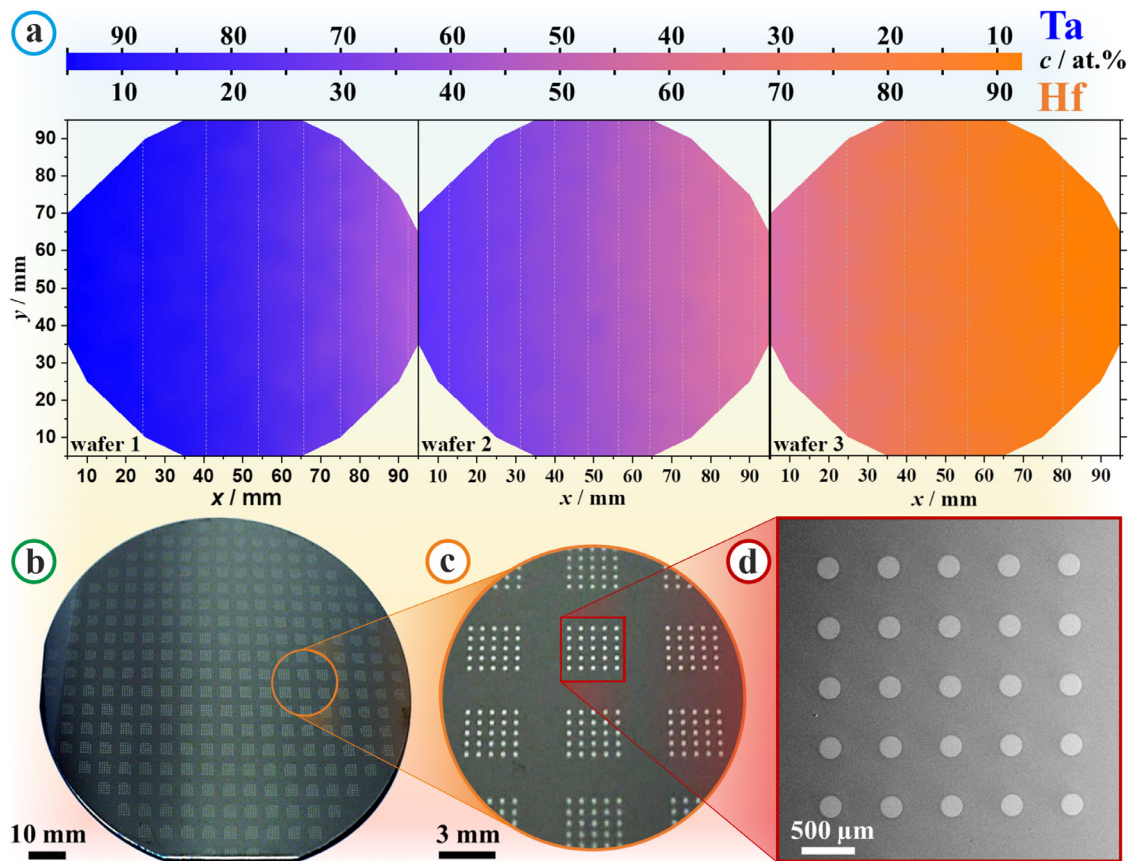


Fig. 2. EDX compositional mapping for the entire Hf-Ta library spread on three 100 mm Si wafers (a), photographs of substrate with finalized devices after the top Pt electrode patterning (b, c) and SEM image of a single anodic memristors cluster (d).

Schematic visualization of the actual Hf-Ta thin film library, immediately after its co-sputtering, is presented in Fig. 2a, where the SEDX mappings of all three wafers defining the entire library are presented. It can be observed that overall the Hf-Ta library has a compositional spread of 87 at.%. Alloys ranging between Hf-8 at.%Ta and Hf-95 at.%Ta are shown in the color-coded compositional bar presented in the figure. Accordingly, the Hf amount in the library varied from 5 to 92 at.%. The compositional spread of each of the three wafers was tuned to partly overlap with its neighbors for some redundancy, allowing a continuous property scan along the library while avoiding unwanted edge effects. From the SEDX mappings, a lateral compositional resolution of $0.3 \text{ at.}\% \text{ mm}^{-1}$ can be calculated. The current work aims at providing information about the memristive behavior of Hf-Ta oxides with as high as possible compositional resolution. However, taking into account the assessed error of the performed EDX analysis, no compositions with a precision better than 1 at.% was considered. Therefore, the obtained compositional resolution is quite convenient since a surface

of more than 3 mm along the compositional gradient, containing a cluster of at least a dozen memristors (see Fig. 2b–d), defines each Hf-Ta alloy (within the estimated 1 at.% error bar).

Following the previous arguments and in order to allow for a reasonable number of identical memristors (for a given Hf-Ta parent metal alloy) the Pt top electrodes were patterned in clusters containing 25 electrodes each. Optical photographs of the electrodes are presented in Fig. 2b,c at different magnifications where the electrode clusters and the spacing between them are easily observable. For increasing the observation resolution, an SEM image of a cluster is presented in Fig. 2d. All Pt top electrodes are identical defining individual memristors belonging to the same Hf-Ta composition. Scanning for compositionally induced changes refers to measurements performed in different clusters along the compositional gradient, while clusters perpendicular to the gradient direction provide memristors with identical compositions. This is indirectly observable also in Fig. 2a. In order to organize and ease the presentation of the obtained results from this work, the en-

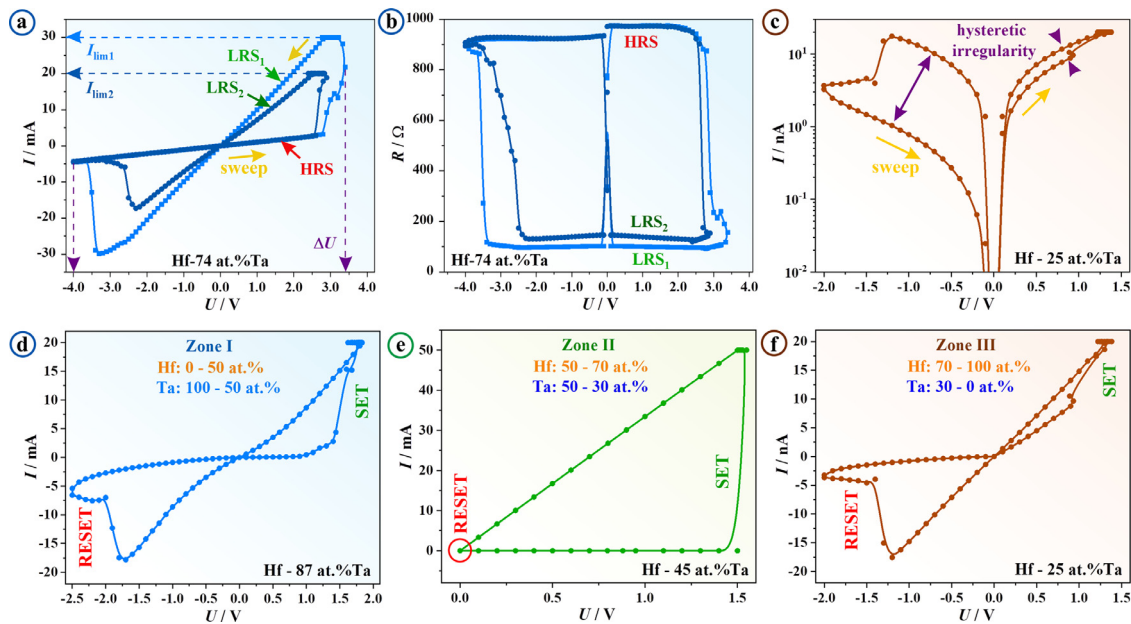


Fig. 3. Exemplifying plots applied to each analyzed memristors along the library: (a) hysteretic memristive I - U curve with identification of relevant parameters and sweep directions used for the entire study, (b) derived R - U curve for resistive states observation and (c) switching curve plotted in logarithmic current scale for hysteretic irregularities observation. (d-f) Representative switching curves for selected memristors defining three compositional zones of interest along the Hf-Ta combinatorial library.

tire Hf-Ta library was divided into three compositional zones that share common memristive behaviors: zone I (< 50 at.%Hf), zone II (50 – 70 at.%Hf) and zone III (> 70 at.%Hf).

3. Results and discussion

3.1. Resistive switching in anodic Hf-Ta memristors

Representation of memristive behavior can be done in different ways for emphasizing various characteristics. These representations are extremely relevant in this study, due to a large amount of data within the whole library that needs to be analyzed in identical ways for multiple devices. In Fig. 3a typical I - U curve is shown as measured on one memristor from the library. Several characteristics, such as sweep direction, voltage and current limits, are indicated in the figure and they are defined in the same manner for all investigated memristors. The total number of investigated memristors was around 300 per wafer. Additionally, at least 10 cycles of I - U sweeps were recorded for each investigated memristor. The HRS and two different LRS levels corresponding to the indicated current limits (compliances) are related to the slopes of the I - U curves due to Ohm's law. However, easier observation of those switching levels can be done in an R - U plot as exemplified in Fig. 3b for the same memristor. Both distinct LRS levels can be better observed and discussed in such a plot. Finally, plotting the I - U data in logarithmic current scale allows better observation of hysteretic anomalies. This is exemplified in Fig. 3c where a hysteretic irregularity can be easily observed for a zone III memristor.

The switching characteristics extracted from the I - U sweeps have been changing within the Hf-Ta compositional spread along the three defined zones. In Fig. 3 d-f representative curves belonging to memristors from each compositional zone are presented. The devices from zones I and III showed bipolar switching behavior, while memristors in zone II resemble unipolar behavior. The differences obtained during I - U sweeps measurements were the main criterium for defining the compositional zones and have been used further in the properties screening. Additionally, in zones I and III memristive forming by positive biasing was nec-

essary, while zone II did not require any forming step. Identification of a region roughly in the middle of the entire compositional spread (50 – 70 at.% Hf), where forming-free devices are observed, is extremely important for material selection during further device implementation in real-life applications. Furthermore, with the increase of Hf amount (> 70 at.%) in zone III (Fig. 3f), the anodic memristors regain the bipolarity but their hysteresis remains strongly irregular, with different polarity dependent HRS values.

The mechanism of the bipolar switching is described as mainly electrical and thermal field-assisted ionic drift inside the oxide layer [6,9]. Thus, the formation and deletion of CFs are based on the electromigration and thermally activated displacement of the same defects (oxygen vacancies) initiating solid-state redox reactions. If in bipolar switching the electric field influence dominates, in unipolar case the redox process is mainly assisted by local Joule heating and quantum effects [6,9]. In other words, the unipolar switching to LRS (set process) or to HRS (reset process) is described as a voltage-controlled breakdown event, which is followed by thermal formation or disruption of CFs [32]. Additionally, it was reported that filamentary regions in unipolar devices can appear as nano-islands rather than the typical continuous filaments observed for bipolar switching [6]. Continuous filaments may be oxidized or reduced due to the enhanced mobility of O species drifting from anode or cathode interface along grain boundaries, linear defects and dislocations [32]. With this regard, it should be expected that different compositions of Hf-Ta parent metal alloys could affect the anodic memristors switching behavior. Therefore, as Fig. 3 shows, mixed oxides-based memristors offer the intrinsic possibility of CF formation assisted by different processes, whose selection is compositionally driven.

Analysis of memristive switching curves for each oxidized Hf-Ta alloy along the library allowed compositional mapping of several relevant memristive characteristics, which are presented in Fig. 4. In part (a) of the figure, the voltage switching characteristics (ΔU) are mapped for the entire library, being extracted from individual I - U plots as indicated in Fig. 3a. The error bars presented are defined empirically by the variations between different devices formed at the same Hf-Ta composition. It can be observed

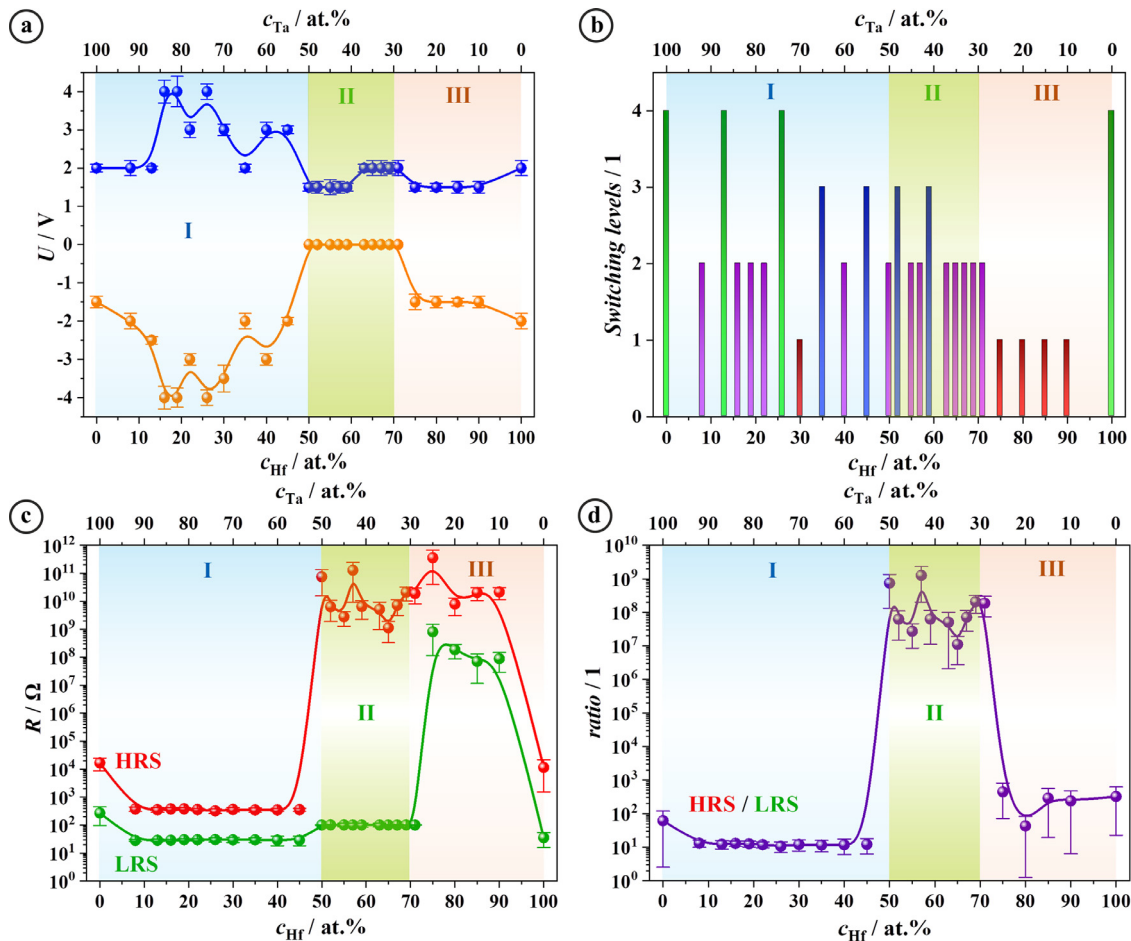


Fig. 4. Compositional mapping in the Hf-Ta system describing anodic memristors forming voltage characteristics (a), number of switching levels (b), values for the high and low resistive states (c) and their ratio (d).

that at the edge of Hf-Ta compositional spread, the behavior of anodic memristors resembles those of devices built on pure Hf or Ta metallic film precursors [27,28]. At low Hf concentrations in zone I, as well as in the entire zone III, anodic memristors were switched bipolarly with ΔU up to ± 2 V, just as in the case of pure Hf or Ta oxide devices anodized in CB as reference. Increasing the Hf concentration above 10 at.% in zone I, the switching voltage range increased reaching ± 4 V for Hf amounts up to 30 at.%, and further decreased toward the initial ± 2 V values at the end of zone I. However, a rather large fluctuation of data can be observed, likely linked to the transition towards zone II.

The switching features of zone II are suddenly pointing towards unipolar characteristics. This compositional range defines a rather unique set of anodic Hf-Ta memristors. Firstly, no memristive forming by biasing the device in a positive direction was necessary for this zone, thus removing a usually required fabrication step. Secondly, memristive switching to LRS (set process) was successful in a quite low positive voltage range (up to 1.5 V for the first half of zone II). Similarly, the switching from LRS to HRS (reset process) was achieved at very low voltage values close to 0 V. Based on the fact that the RESET process is accomplished by bringing bottom and top electrodes at the same potential, one could doubt a unipolar switching behavior [33]. However, precisely this behavior was recently explained by the coexistence of non-volatile threshold and memristive characteristics, in which a self-reset process is achieved by short-circuiting the bottom and top electrodes in similar experimental conditions using HfO_2 [34]. In addition, the unipolar behavior was justified by the presence of nano-inclusions

inside HfO_2 , which are reconfirmed in the present study (discussed further in the TEM analysis) [6,34]. These characteristics are making this mixture of oxides very attractive for low voltage applications, e.g., selector devices [35,36]. At the same time, the possibility of multifunction applications based on mixing a volatile selector with a nonvolatile memory is promising and may expand towards neuromorphic applications [34]. It is also relevant to note here that the coexistence of threshold and memory is studied for different materials [37–39].

Multi-level switching is a crucial memristive parameter to be evaluated along the Hf-Ta library due to its importance as a memory characteristic, particularly for neuromorphic applications [40]. The existence of a high number of distinguishable resistance levels allows the simulation of an analog behavior of a memristive device that can store more than one bit per cell [41,42]. The compositional mapping of the anodic memristors switching levels along the Hf-Ta library is presented in Fig. 4b. Generally, devices from zone I were switched successfully at more than 2 levels, 4 levels being observed for several Hf-Ta compositions together with the pure Ta and Hf oxide reference memristors. Most anodic memristors belonging to zone II had 2 distinguishable switching levels, while in zone III only one level could be identified. All these switching features along the Hf-Ta compositional gradient are pointing out that memristive devices based on alloys containing a lower percentage of Hf (zone I) would provide better memory characteristics, being potential candidates for ReRAM applications. However, memristive devices in zone II showed simpler and electroforming-free unipolar switching, which combined with their

lower operating voltage range, may be considered as a prominent advantage for applications such as selector device, in spite of their smaller number of switching levels.

In Fig. 4c the ohmic values for both LRS and HRS are plotted as compositional mapping along the entire Hf-Ta library. The data was collected from each addressed memristor in a manner similar to the ones exemplified in Fig. 3a,b. As it can be seen (Fig. 4c), LRS values for alloys with Hf content below 70 at.% are very close to those of memristors based on pure Hf and/or Ta. Within zone I and zone II these values are quite stable in the range of 100 Ω and the threshold between the zones is well marked by a small LRS change. Overall the LRS is stable and reproducible over the compositional range of zones I and II. The LRS values in zone III are much higher, reaching 1 G Ω and showing bigger variability, as visualized by the larger error bars in the graph. This is a first indication that mixed oxides in zone III may not be well suited for memristive applications.

Additionally, in Fig. 4c the HRS values are compositionally mapped and their behavior differs drastically from the LRS ones. Even though a slight decrease of HRS for alloys in zone I is still recognizable being compared with pure Ta or Hf oxides, their values remained stable along the entire zone at values below 10³ Ω . The transition between zones I and II is emphasized by a sudden increase of HRS values by at least 6 orders of magnitude. Devices based on alloys in zone II showed HRS values ranging from 10⁹ Ω to almost 10¹¹ Ω . Further increasing the Hf concentration along the library, a significant drop of the HRS values down to 10⁴ Ω (for HfO₂ grown in CB) can be observed for anodized alloys in zone III.

For real applications though, one important factor characterizing a memristor is the ratio between HRS and LRS, which provides a measure for the resistive switching efficiency evaluation. The HRS/LRS ratios measured along the entire library are compositionally mapped in Fig. 4d. The performance of memristors from zone I is worse compared with pure Hf or Ta oxides, with a ratio slightly above 10. The zone II devices showed significantly increased HRS/LRS values reaching in excess of 10⁷. Such strong differentiation between resistive states may be extremely useful in low voltage applications by eliminating possible uncertainties related to the state reading of a device. Additionally, forming-free and low switching voltage features increase the compositional relevance of zone II. As the Hf amount increases further along the Hf-Ta library, in zone III HRS/LRS ratios with high instabilities were found. Combined with the previously observed behavior of both states, this renders zone III as inappropriate (from an electrical point of view) for memristive applications and thus it will not be pursued further in the frame of this work.

3.2. Endurance and retention of anodic Hf-Ta memristors

Endurance and retention tests performed on devices along the Hf-Ta library resulted in similar behaviors for oxides belonging to each of the compositional zones previously defined. Fig. 5 shows retention and endurance measurements representative for the compositional zones I (a and b) and II (c and d). The composition of each Hf-Ta alloy chosen to represent each zone is given in the figure. Testing in zone III did not lead to meaningful reproducible results, as expected from the overall electrical behavior previously discussed. Cycle-to-cycle variability intervals for both resistive states are shown in Fig. 5 by orange-colored confidence bands, as empirically defined by analyzing all performed tests in each zone. The intervals are based on measurement scattering extracted from up to 25 different devices, excluding extreme values.

Extremely stable LRS values were confirmed up to a few millions of cycles of retention testing in zones I and II. During endurance testing of memristors from zone I, LRS values started

to increase when reaching 10⁵ cycles, whereas HRS values remained rather constant in a similar ohmic range as during retention testing. Consequently, HRS/LRS ratio became lower than 10 after 10⁵ cycles and the tested memristors reached the end of their lifetime. The HRS values in zone I have a maximum absolute error in the range of 150 Ω , as easily calculated by observing the retention confidence band (slightly larger compared to the endurance band). The mixed oxides from zone I show similar behavior as pure Hf or Ta oxides with HRS/LRS ratio in the range of one order of magnitude for at least 10⁵ cycles [27,28].

The HRS values measured during retention and endurance testing of the devices in zone II increased by several orders of magnitude reaching approximately 10¹⁰ Ω . In both tests, cycle-to-cycle variability in the range of 2 orders of magnitude was observed (Fig. 5c,d). At the same time, this may be deemed acceptable considering possible higher noise sensitivity appearing due to very low currents passing through devices. The reset mechanism for unipolarly switched devices has been recognized as a self-accelerated process, which can cause different cycle-to-cycle HRS values due to the limited control of switching to HRS [43]. Additionally, in zone II the HRS/LRS ratio with lower cycle-to-cycle variability was improved by several orders of magnitude as compared to devices from zone I or anodic memristors based on pure Hf or Ta [18,27,28]. Such improvement is noticeable even with respect to Ta and Hf oxide devices fabricated by sputtering [44,45] or atomic layer deposition [46]. The anodic memristive devices in zone II remarkably show at least 7 orders of magnitude difference between HRS and LRS for more than 10⁶ switching/writing or reading cycles.

In general, the results for zone I and II memristors match well the compositional mappings from Fig. 4c,d suggesting that the values presented there (measured from the first switching) could be safely assumed as constant for each zone for a high number of cycles. Additionally, cell-to-cell variability is indicated by error bars and confidence bands in both Figs. 4 and 5, whereas typical cycle-to-cycle variability is exemplified in Fig. 5 and supplemental Fig. S1.

Usually, pure anodic Hf and Ta memristors are reported to withstand 10⁵ endurance and retention cycles without failure, due to a sudden increase of HRS conductivity and decrease of LRS conductivity. Previous reports explained such events as an undesirable consequence of the electroforming step, which dictates the shape, size and stability of CFs and thus memristive performance [47]. Additionally, the electrolyte selection for anodization plays a role in the final memristive behavior [27,28]. In this regard, the idea of electroforming-free memristors is extremely attractive because this will improve the uniformity and stability of devices. Moreover, the instability and thickening of the CFs with cycling were reported to appear due to the enhancement of effective tunneling area or additional O vacancies diffusion into the CFs rupture region [47,48]. Since these devices were also switched unipolarly, this may point towards the formation of one and more stable filament which may be less prone to the above-described events [47]. In contrast, memristors from zone I were switched bipolarly, in higher voltage ranges, which could be justified by the formation of multiple parallel CFs, with one main thicker CF [46]. This switching mechanism based on several CFs was reported as less stable. At the same time, it may also clarify the observed sudden increase of the LRS resistance at 10⁵ cycles during the endurance performance (Fig. 5b) [47,48].

3.3. Composition and chemical states analysis of anodic Hf-Ta memristors

The in-depth compositions of two Hf-Ta anodic memristors corresponding to the relevant compositional zones I and II (Hf-70 at.%)

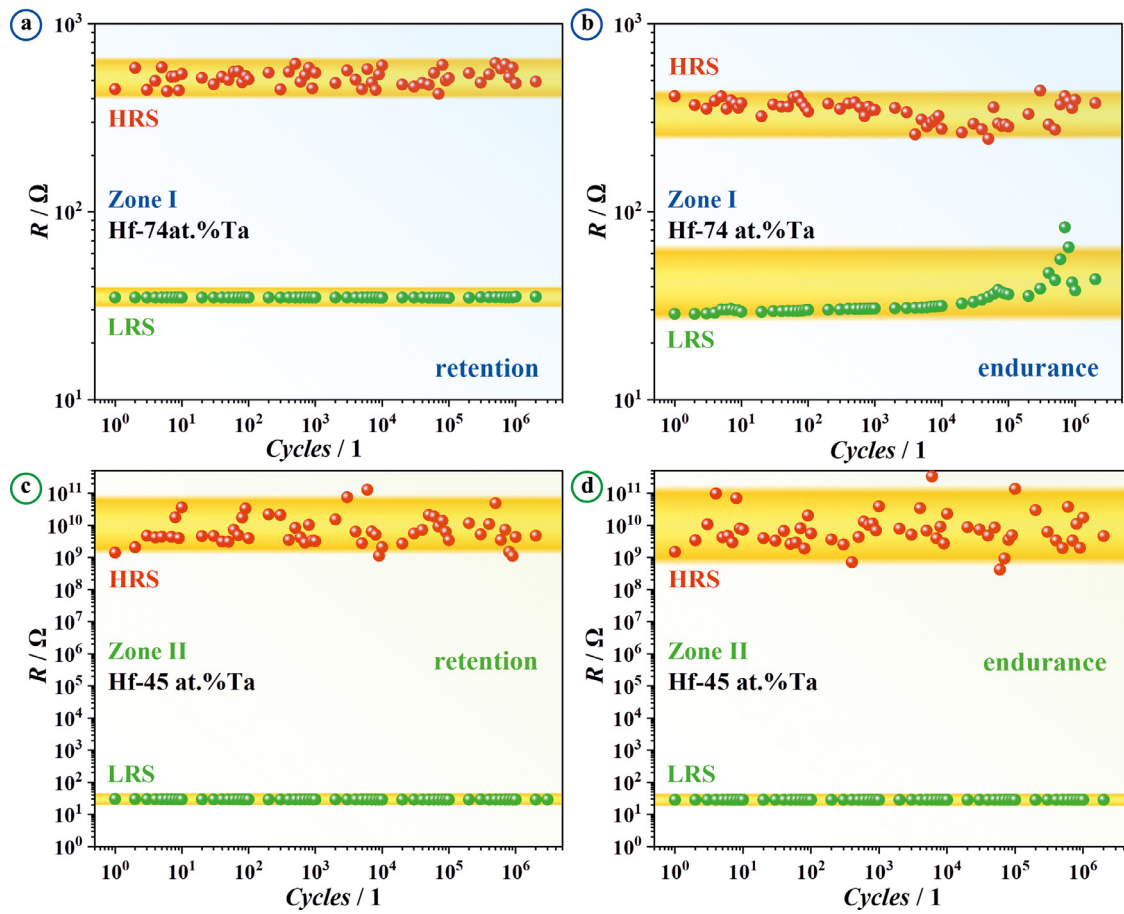


Fig. 5. Retention and endurance testing representative curves selected for compositional zones I (a, b) and II (c, d) (For interpretation of the references to color in this figure, the reader is referred to the web version of this article.).

Ta and Hf-35 at.% Ta, respectively) were analyzed by XPS depth profiling, and the results are presented in Fig. 6. The evolution of the measured Ta 4f - Hf 4f region for successive sputtering steps is displayed in Fig. 6a and b for zones I and II, respectively. In both cases, the presence of oxidation states of Hf and Ta in the mixed oxides is evidenced. The surface region of both oxide types (up to a sputter depth of roughly 3–5 nm) is strongly enriched in Hf (as compared to the oxide interior), confirming earlier results [22]. This is due to preferential sputtering of O, an artifact commonly observed for oxide compounds. Fortunately, the relative sputtering rates of Ta and Hf are similar and, consequently, the Hf/Ta atomic ratio in the oxide layers should be unaffected by preferential sputtering effects.

As follows from the recorded depth profiles in Fig. 6c,d, the interior region of the zone I and zone II oxides (at about 5 min of sputtering) is characterized by Ta/Hf atomic ratios of about 3.3 and 0.3, respectively. The metallic peak contributions from the alloy substrate appear at a lower sputtering depth for zone I oxide, which indicates that the zone I oxide is thinner than the zone II oxide (assuming a similar sputter rate for both oxide types), later testified by cross-sectional TEM (see the supplemental Fig. S2). Such a dependence of the oxide layer thickness on the parent alloy composition is expected due to the compositional dependence of the oxide formation factors in the Hf-Ta system [22].

Sputtering effects hinder a true chemical state analysis of Ta and Hf in the oxide layer interior by classical XPS depth profiling. To address this challenge, a bulk-sensitive HAXPES analysis of the as-deposited oxide layers using a hard Cr-K α X-ray source was performed and the results are presented in Fig. 7a. This allows in-

vestigating the unperturbed mixed Ta-Hf oxides. The Ta 4f - Hf 4f regions of the as-deposited oxide types and reference oxides of HfO₂ and Ta₂O₅, as measured with the Cr-K α source, were investigated. A comparison of the measured XPS spectra after 4 sputter cycles with the HAXPES spectra of the unperturbed oxides characteristic to zones I and II are shown in Fig. 7b and 7c, respectively. While dominant single valence states are observed for Ta and Hf in the unperturbed oxide layer (without sputtering using the Cr-K α source), a clear shift of the original peak positions with additional substoichiometric peak contributions appears in the perturbed oxide layer (after sputtering and measured using the Al-K α source). Notably, a minor Ta metallic contribution from the alloy substrate is probed for the zone I mixed oxide in its unperturbed state, which is absent in the corresponding spectra of the zone II mixed oxide. This is also in consonance with the fact that zone I oxide layer is thinner than the zone II mixed oxide layer (i.e. the HAXPES analysis non-destructively probes across the entire oxide layer). The StrataPHI layer reconstruction for both oxide types (assuming an in-depth homogeneity) results in nominal bulk compositions of 20 at.% Ta - 13 at.% Hf - 67 at.% O for the zone I oxide and 9 at.% Ta - 29 at.% Hf - 62 at.% O for the zone II oxide. The respective oxide-layer thickness for the zone I oxide is 23 nm (note: the layer thickness of the zone II oxide cannot be resolved by the StrataPHI reconstruction, since a metallic substrate signal is not detected).

In zone I memristors the amount of anodized Hf exceeds the amount of metallic Hf in the parent alloy by at least 5 at.%, while in zone II the memristors stoichiometry is shifted by more than 10 at% toward Hf. This is due to the competition between Hf and

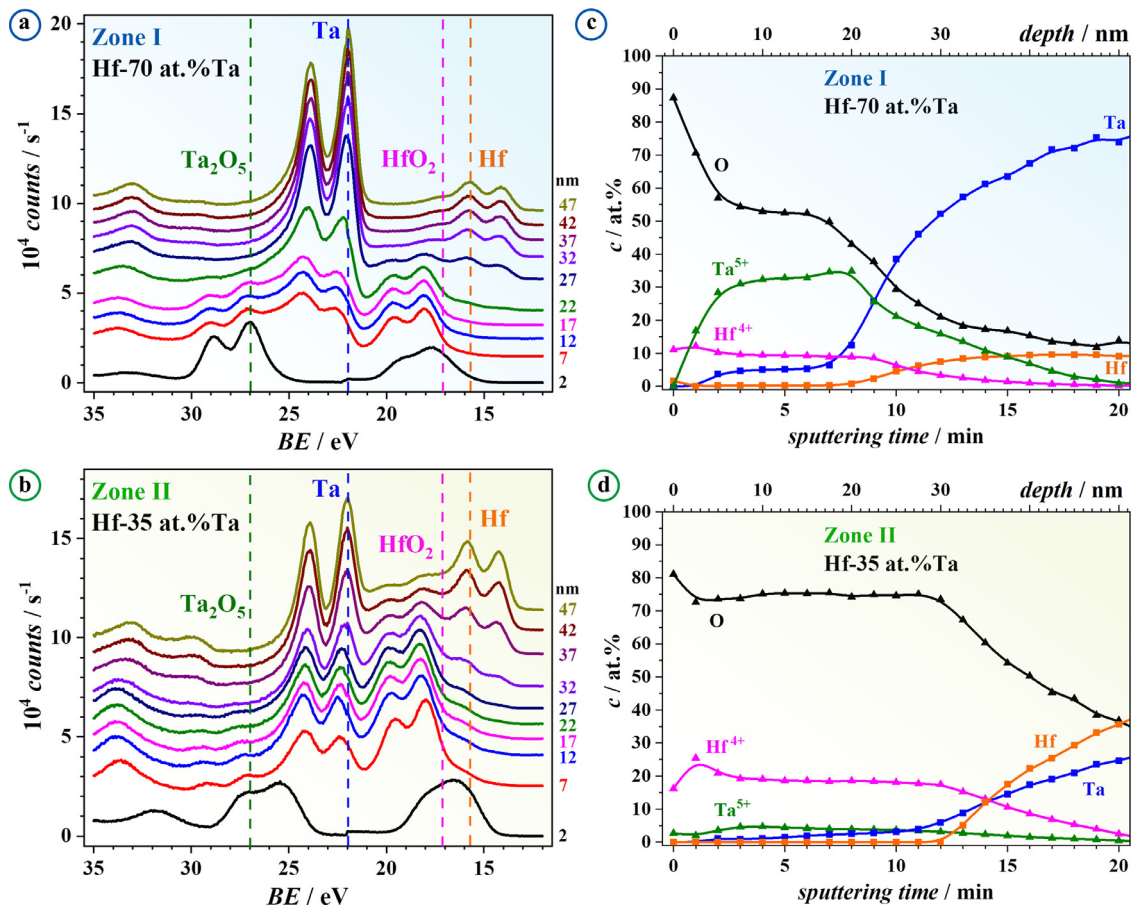


Fig. 6. XPS spectra of the combined Ta 4f – Hf 4f region (dashed lines) as recorded at various sputter depths for anodic oxides representative for zone I (a) and II (b). The reconstructed sputter depth profiles are shown in panels (c, d).

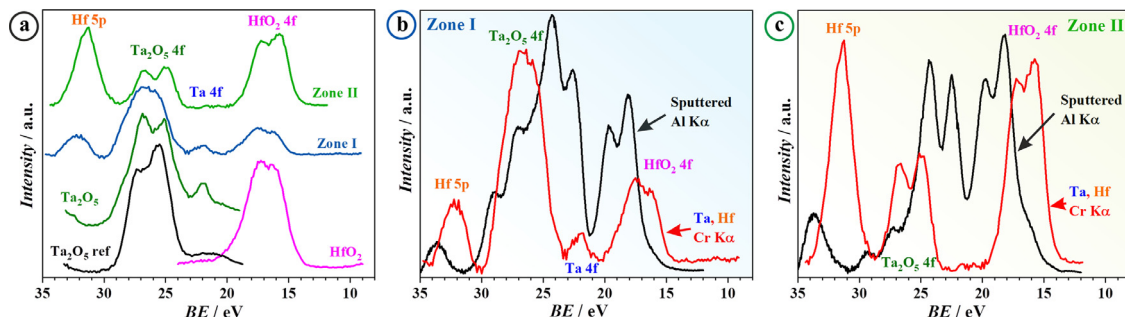


Fig. 7. HAXPES spectra of pure anodic oxides, zone I and II oxides and standard Ta_2O_5 (a) and comparison of XPS (after sputtering) and HAXPES results for oxides from zones I (b) and II (c).

Ta during their high field ionic migration [22]. The stronger Hf enrichment of oxides from zone II (compared to zone I) is primarily triggered by the Hf/Ta ratio and may play a role in the much better memristive behavior of devices in this compositional region. Having an ionic transport number close to zero, Hf will practically be immobile during anodization as reported to its initial position in the metallic matrix, while the more mobile Ta will oxidize faster expanding the oxide volume inside the electrolyte. However, the O anion moving in the opposite direction is much faster than both cations and thus Hf will get a chance to oxidize as well. The resulting electrical peculiarities and overall characteristics of the final oxide are a complex combination of factors primarily triggered by the “ideal” Hf/Ta atomic ratio. The simulated oxide layer thickness is in excellent agreement with the value expected from electrochemical and TEM data.

The local chemical states of the anions and cations in a given oxide compound can be evaluated from the so-called (modified) Auger parameter (AP), as measured by XPS/HAXPES [49,50–52]. Auger transitions are a unique probe of the strength of on-site electron correlation [53]. Consequently, the AP shift between two different local chemical states of an atom in the solid is a direct measure of the difference in electrical screening efficiency around the localized core hole(s) of the core-ionized atom (as created in the photo- or Auger process) [54]. The AP of O (i.e. O 1s + O KLL), Hf and Ta (i.e. Hf 4d + Hf LMM / Ta 4d + Ta LMM) in the zone I and II oxides were evaluated from the respective photoelectron and Auger lines, as recorded with the soft Al and/or hard Cr X-ray sources [49]. Notably, the O1s, Hf 4d and Ta 4d core levels can be accessed with both the Al and Cr source (corresponding to different probing depths), while the respective LMM Auger

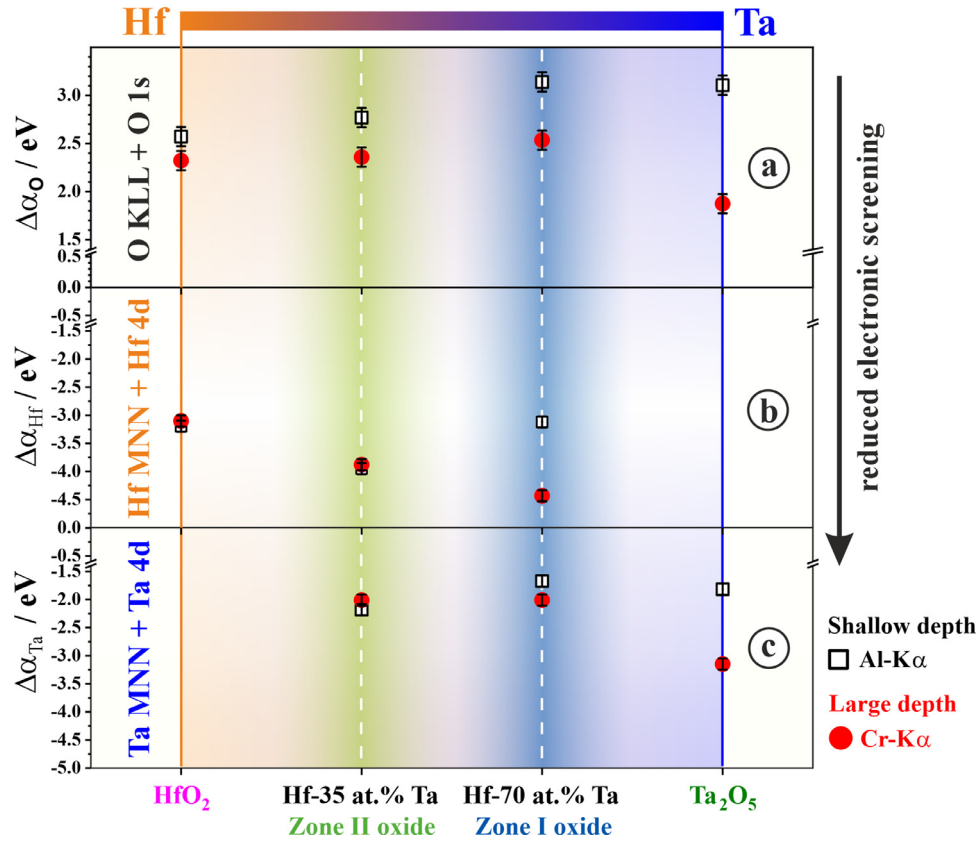


Fig. 8. O and Ta, Hf Auger parameter shifts, $\Delta\alpha$, as a function of the Ta content in the mixed oxides, as well as in the respective pure oxides. The values of $\Delta\alpha_O > 0$ are referenced to that of O in H_2O , whereas the values of $\Delta\alpha_{\text{Hf}} < 0$ and $\Delta\alpha_{\text{Ta}} < 0$ are referenced with respect to their pure metal. The markers with open squares and solid circles correspond to the $\Delta\alpha$ shifts at a shallow and large probing depths, as determined from the measured core-level BE values recorded with the soft Al-K α or the hard Cr-K α X-ray source, respectively (note: the probing depth of the respective Auger lines is independent of the photon source).

lines can only be excited using the Cr source (at constant probing depth)[49]. The as-obtained AP values (denoted α), are independent of the incident photon energy and of charging effects [50–52].

For chemical state analysis, α values are generally referenced to a well-defined reference state, α_{ref} . The value of $\Delta\alpha = \alpha_{\text{ref}} - \alpha$ then corresponds to the difference in the local electronic polarizability between the core-ionized atom in the studied compound with respect to its reference state, i.e. $\Delta\alpha = -2 \cdot (R_{\text{ref}}^{\text{ea}} - R^{\text{ea}})$, where $R_{\text{ref}}^{\text{ea}}$ and R^{ea} denote the respective extra-atomic relaxation or polarization energies. The major contribution to R^{ea} is due to the electron response of the local chemical environment of the core-ionized atom upon creation of a core-hole or of two core-holes in the photo-ionization and the Auger process, respectively. This implies that, for a free atomic or ionic species, $R^{\text{ea}} \equiv 0$. The Auger parameter shift of O in oxide compounds, on the one hand, is commonly referred to the H_2O molecule ($\alpha_{\text{H}_2\text{O}} = 1038.5$ eV; as atomic O^{2-} does not exist) [55] and thus $\Delta\alpha_O = 2R_O^{\text{ea}} > 0$. The Auger parameter shift of the cation(s), $M^{\delta+}$, in oxide compounds, on the other hand, can be most easily referred to their respective pure metal, M^0 . The core-ionized atom in metal is very well screened as compared to the respective atom in the oxide compound (i.e. $R_{M^0}^{\text{ea}} \gg R_{M^{\delta+}}^{\text{ea}}$) and thus $\Delta\alpha_{M^{\delta+}} = -2 \cdot (R_{M^0}^{\text{ea}} - R_{M^{\delta+}}^{\text{ea}}) < 0$.

The $\Delta\alpha$ shifts for O, Ta and Hf in the zone I and II oxides, as well as in the respective pure oxide phases Ta_2O_5 and HfO_2 , have been plotted as a function of the Ta content (i.e. from pure $\text{Ta}_2\text{O}_5 \rightarrow \text{Hf-35 at.\% Ta} \rightarrow \text{Hf-70 at.\% Ta} \rightarrow \text{HfO}_2$) in Fig. 8a–c. The markers with open squares and solid circles correspond to the $\Delta\alpha$ shifts at shallow and large probing depths, as determined from the measured core-level BE values recorded with the soft Al-K α or the hard Cr-K α X-ray source, respectively. Any deviation between the

$\Delta\alpha$ values at shallow and large probing depths hints at a gradient in the local chemical state of the respective atoms as a function of depth below the oxide surface. As evidenced from the sputter-depth profiles of Fig. 6c,d, the zone I and II oxides are strongly enriched in Hf at their surfaces. Therefore, in the following, only the chemical states at large probing depths (solid cycles, in red) will be discussed in detail.

As follows from Fig. 8a, the value of $\Delta\alpha_O$ for the zone I and II oxides (at large probing depth) is similar to that of O in HfO_2 and considerably higher as compared to Ta_2O_5 . This implies that the O ions in the Ta_2O_5 , on average, become more effectively screened upon mixing with Hf. In other words, the O electronic polarizability is higher for the mixed oxide in zone II. This is in line with the much lower electronegativity, lower electronic conductivity and higher refractive index of HfO_2 as compared to Ta_2O_5 (note: according to the Clausius-Mossotti relationship, a rise of the refractive index leads to increased molar polarizability and hence to increased electronic polarizability of the first-neighbor ligands of the O atom). Growth of the Hf content also results in the (near-linear) increase of the electronic polarizability (i.e. an increase of $\Delta\alpha_{\text{Hf}}$) around the mixed Hf cations (Fig. 8b). Accordingly, the local electronic polarizability of Ta in the zone I and II oxides are higher as compared to that in Ta_2O_5 , although very similar for the zone I and zone II oxides (Fig. 8c). This suggests that the improved memristor performance for the zone II oxide composition (as compared to the zone I oxide composition) is likely related to the lower electronic polarizabilities (screening efficiencies) of O and Hf when applying an external electrical field upon cycling. In this regard, it is also emphasized that the local chemical state of Hf is near-identical at shallow and larger probing depths for zone II oxide, but very

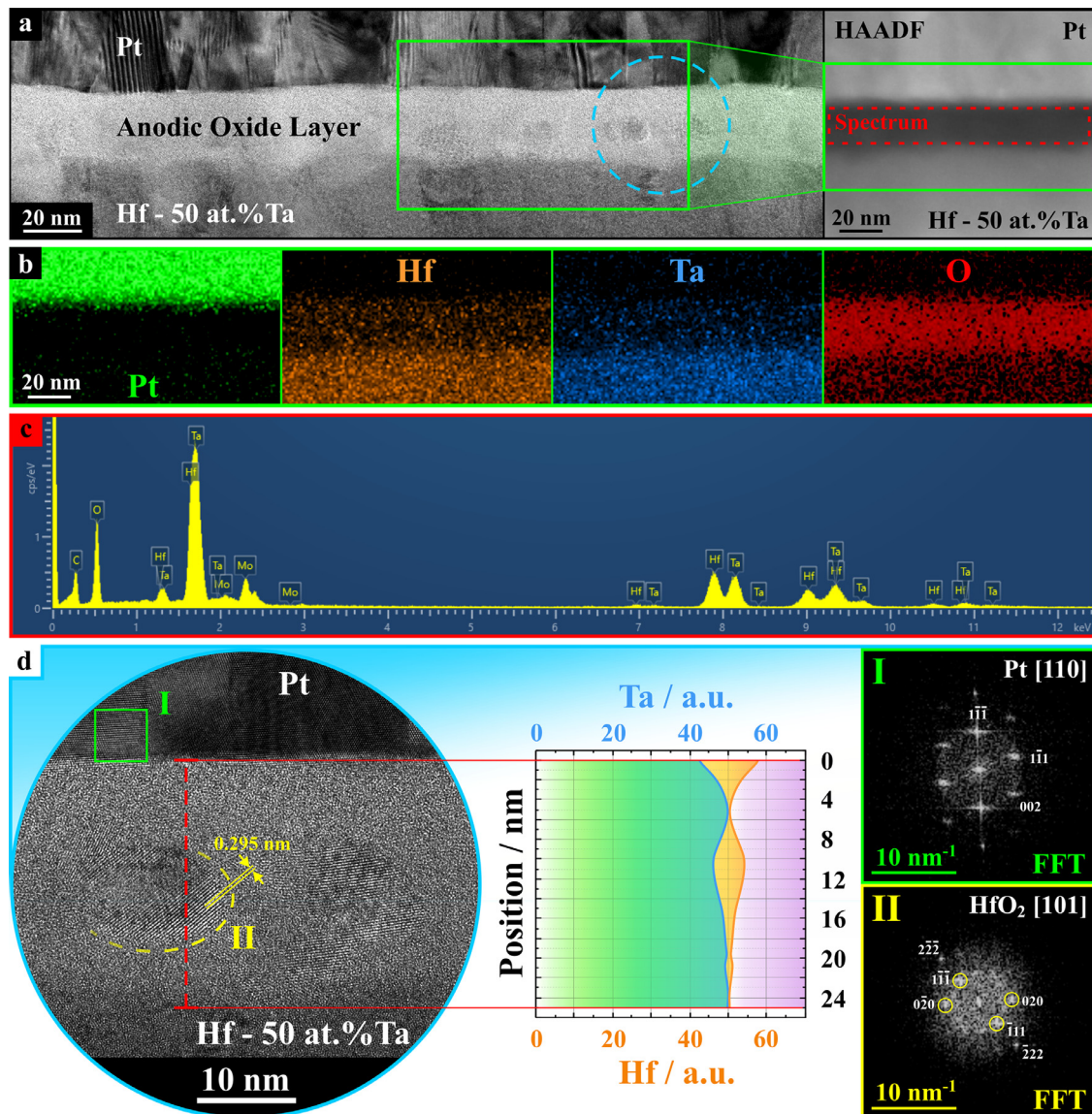


Fig. 9. Results of the TEM investigation of zone II memristor cross-section. (a) TEM along with HAADF STEM imaging of the anodic oxide layer between Pt and Hf-Ta electrodes. (b) STEM EDX compositional maps of the region designated with a green frame in (a). The maps were reconstructed using L series of characteristic X-Ray spectrum for Pt, Hf and Ta and K series for O. (c) Map sum spectrum corresponding to the anodic oxide layer region (highlighted with a red dashed frame in (a)). The Mo peaks correspond to the TEM grid. (d) HRTEM snap of the area shown with blue dashed circle in section (a) accompanied by through-thickness Hf-Ta ratio analysis. FFT patterns of regions I and II are presented in the corresponding insets (For interpretation of the references to color in this figure legend, the reader is referred to the web version of this article.).

different for zone I oxide (compare solid circle and open squares in Fig. 8a and b). This indicates that zone I oxide is much more heterogeneous in composition, as also evidenced from the sputter-depth profiling. The more homogeneous composition of the zone II oxides could hint at a minimum in the Gibbs energy of formation of a mixed (Hf, Ta)-oxide for Hf contents in the range of 50–70 at.%, similarly to the observed formation of amorphous (Al, Zr)-oxides with a well-defined stoichiometry [56]. Such a minimum in the Gibbs energy of formation of the mixed (Hf, Ta)-oxides would also rationalize the very stable cycling behavior as observed for the zone II oxides in this study.

3.4. Structure of anodic Hf-Ta memristors

To bring more light to the fundamentals behind superior memristive performance specific for zone II devices, meticulous investigation of their structural peculiarities is vital. To address this chal-

lenge, a thorough TEM analysis has been performed on the typical zone II and zone I memristors after *I-U* cycling tests (low magnification TEM images showing a general view of the MIM layered structure could be found in Fig. S2). The in-detail results on the zone II memristor are summarized in Fig. 9. Part (a) of the figure shows an overall TEM image of the MIM layers. It reveals an approximately 25 nm thick anodic oxide layer sandwiched between Pt (top) and Hf-Ta alloy (bottom) layers. The observed polycrystalline structure of the metal films with distinguishable grains is expected considering the formation approach, while the oxide layer looks quasi-amorphous. Additionally, one can see a distinct feature of the oxide layer, which looks like a series of peculiar crystalline entities and will be discussed later (Fig. 9a). The results of the TEM investigation of a typical zone I memristor are provided in the supplemental Fig. S3 for comparison. STEM EDX mapping was performed for gaining general information about through-thickness components distribution complementing the quantitative HAXPES

chemical analysis discussed above. The assessed EDX measurement error was ± 1.5 at.% [57]. The color-coded elemental maps of the green framed region are provided in Fig. 9b. The bottom electrode composition was estimated to be Hf-50 at.%Ta (50/50 ratio). This value is in full consonance with SEDX screening data presented in Fig. 2a and is defined by the position of the chosen memristor in the library. From the point of simplicity and to avoid ambiguity of O quantification in TEM lamellas via EDX, the Hf/Ta ratio will be further used for the results presentation. It is worth mentioning that the Hf/Ta ratio in the anodic oxide layer deviated from the one of the parent metal layer and was measured to be 53/47, the corresponding map sum spectrum could be found in Fig. 9c. Moreover, this ratio is not uniform. Applying a multiple line scan approach, the distinguishable range of through-thickness Hf/Ta ratios from $\approx 52/48$ at the bottom electrode interface up to $\approx 54/46$ in the vicinity of the Pt electrode could be revealed. The formation of this gradient is predicted and can be unambiguously justified by comparably lower Hf ionic mobility (compared to Ta) during the anodization process and is in agreement with available findings in the field [22].

HRTEM analysis has been fulfilled with the principle focus on the structural features in the anodic oxide layer. Fig. 9d shows the enhanced image of the region marked with the blue circle in Fig. 9a revealing a quasi-amorphous oxide layer embedded with crystalline regions. Rigorously performed multiple through-thickness EDX line scanning in this area (designated with a dashed red line) confirmed a slightly increased Hf to Ta content ratio attributed to the specific crystallite location (see the inset in Fig. 9d). However, it is worthy to note that assessed EDX measurement error allows stating the relative components ratio evolution only and rules out faithful quantitative chemical probing. Consequently, fast Fourier transform (FFT) analysis has been systematically applied to the distinct sample regions for phases' confirmation. To enhance the accuracy of quantification during image processing, a Pt grain aligned along the [110] zone axis in the polycrystalline Pt layer (region I in Fig. 9d), was used as an intrinsic reference for calibration [58]. Related FFT pattern could be found in the inset. Following this approach, the *d*-spacings of a crystallite entity of region II were estimated to be 0.295 nm and 0.257 nm. These values are in good correlation with {111} and {002} spacings of HfO₂ according to available crystallographic datasets [59,60]. Other possible candidates, such as Hf, Ta and Ta₂O₅ were also checked but have not matched.

Considering the above-mentioned results and the confirmed free-forming nature of zone II memristors, it can be suggested that the observed HfO₂ crystalline regions were formed through self-assembly of matter during the anodization process under a high field. The particularities of the oxide growth are governed by the components' concentration of a given Hf-Ta alloy and, consequently, by a competitive migration of constituents' ions toward the electrolyte interface where O is found. However, further investigation of the anodic oxide formation process is still actual for unrevealing the full dynamic of the crystallite formation. At the same time, these HfO₂ crystallites embedded in a quasi-amorphous oxide layer likely play a key role in the general zone II memristor improved performance, enhanced stability, and highly uniform resistive switching (in contrast to the zone I devices presented in supplemental Fig. S3). This conclusion is in line with recent outcomes and is supported by the chemical analysis of the oxides [61,62]. According to the authors' approach [61], HfO₂ films were embedded with patterned highly ordered metal nanoparticles (NPs) arrays, which provided short circuit paths in an insulating layer and, in this manner, defined separate and distinct positions favorable for CFs formation. A similar effect was reported for Al₂O₃ based memristors with embedded Ag NPs [62]. In line with these findings, the locally enhanced electric fields along NPs promote oxy-

gen vacancy generation and accumulation, drastically reduce the switching voltages and improve HRS/LRS ratio [62]. The CFs formation and rupture randomness was significantly decreased due to the seed effect, leading to better device stability. In this regard, HfO₂ crystallites embedded in the quasi-amorphous anodic oxide layer may have a similar effect. However, our knowledge of the electrokinetic properties of HfO₂ compared with the surrounding mixed oxide matrix is still scarce, especially at the nanoscale. Despite it is believed that this difference should not be as dramatic as in the 'metal nanoparticles – oxide matrix' case, it could be significantly enhanced due to a size effect. Consequently, deeper insights into the phenomenon are essential and will be addressed in the frame of upcoming investigations.

4. Conclusions

In the current work, a compositional range producing enhanced anodic memristors in the Hf-Ta system was identified using combinatorial screening. A co-sputtered Hf-Ta thin film library was anodized and memristive devices were fabricated on its surface by patterning Pt top electrodes. After electrical characterization of devices positioned at various locations along the compositional spread, three relevant compositional zones sharing common features were identified. A low-Hf containing zone did not feature any memristive improvements compared to Ta₂O₅, while a high-Hf containing zone had extremely poor memristive behavior. Only a middle region, with Hf concentration between 50 and 70 at% presented anodic oxides with exceptional memristive qualities. Ratios between resistive states exceeded 8 orders of magnitude, while retention and endurance testing were successful for more than one million cycles. Memristors in this region are unipolar, forming-free, while all other neighboring compositions, including pure oxides, are bipolar. Soft and hard X-ray photoelectron spectroscopy was used for the chemical analysis of these oxides. An enrichment of Hf species close to the surface of anodic oxides was evidenced due to very different ionic transport numbers of Hf and Ta competing for O during the anodic oxide formation. By combining soft and hard X-ray photons it was found that the unipolar Hf-Ta anodic memristors have an in-depth homogeneous local chemical state of Hf and lower electronic polarizabilities for O and Hf. This is believed to be beneficial for the device's endurance and retention performance. The unipolar character and switching stability are linked to the presence of HfO₂ crystallites embedded into an amorphous mixed oxide matrix, as evidenced by transmission electron microscopy.

Data availability

The raw/processed data required to reproduce these findings cannot be shared at this moment as the data also forms part of an ongoing study.

Declaration of Competing Interest

The authors declare that they have no known competing financial interests or personal relationships that could have appeared to influence the work reported in this paper.

CRediT authorship contribution statement

Ivana Zrinski: Conceptualization, Data curation, Formal analysis, Investigation, Validation, Writing – original draft, Writing – review & editing. **Alexey Minenkov:** Conceptualization, Data curation, Formal analysis, Investigation, Methodology, Validation, Visualization, Writing – original draft, Writing – review & editing. **Claudia Cancellieri:** Data curation, Formal analysis, Investigation, Validation, Writing – original draft, Writing – review &

editing. **Roland Hauert**: Formal analysis, Investigation, Validation, Writing – review & editing. **Cezarina Cela Mardare**: Investigation, Methodology, Validation, Writing – original draft, Writing – review & editing. **Jan Philipp Kollender**: Methodology, Validation, Writing – original draft. **Lars P.H. Jeurgens**: Methodology, Resources, Validation, Writing – review & editing. **Heiko Groiss**: Resources, Validation, Writing – review & editing. **Achim Walter Hassel**: Methodology, Resources, Validation, Writing – review & editing. **Andrei Ionut Mardare**: Conceptualization, Data curation, Formal analysis, Funding acquisition, Investigation, Methodology, Project administration, Resources, Software, Supervision, Validation, Writing – original draft, Writing – review & editing.

Acknowledgments

This research was funded in whole, or in part, by the Austrian Science Fund (FWF) [P32847-N]. For the purpose of open access, the authors have applied a CC BY public copyright license to the Accepted Manuscript version arising from this submission. Additionally, the financial support by the Austrian Federal Ministry for Digital and Economic Affairs, the National Foundation for Research, Technology and Development, and the Christian Doppler Research Association is gratefully acknowledged for financing the “Christian Doppler Laboratory for Nanoscale Phase Transformations”. Moreover, the authors acknowledge the Swiss National Science Foundation (SNSF) Research equipment (R'Equip) grant no.182987 for partly supporting this research.

Supplementary materials

Supplementary material associated with this article can be found, in the online version, at doi:[10.1016/j.apmt.2021.101270](https://doi.org/10.1016/j.apmt.2021.101270).

References

- [1] K. Oka, T. Yanagida, K. Nagashima, T. Kawai, J.S. Kim, B.H. Park, Resistive-switching memory effects of NiO nanowire/metal junctions, *J. Am. Chem. Soc.* 132 (2010) 6634–6635, doi:[10.1021/ja101742f](https://doi.org/10.1021/ja101742f).
- [2] T. Ahmed, S. Walia, E.L.H. Mayes, R. Ramanathan, P. Guagliardo, V. Bansal, M. Bhaskaran, J.J. Yang, S. Sriram, Inducing tunable switching behavior in a single memristor, *Appl. Mater. Today* 11 (2018) 280–290, doi:[10.1016/j.apmt.2018.03.003](https://doi.org/10.1016/j.apmt.2018.03.003).
- [3] C.Y. Lin, Y.T. Tseng, P.H. Chen, T.C. Chang, J.K. Eshraghian, Q. Wang, Q. Lin, Y.F. Tan, M.C. Tai, W.C. Hung, H.C. Huang, W.D. Lu, S.M. Sze, A high-speed MIM resistive memory cell with an inherent vanadium selector, *Appl. Mater. Today* 21 (2020) 100848, doi:[10.1016/j.apmt.2020.100848](https://doi.org/10.1016/j.apmt.2020.100848).
- [4] L. Liang, K. Li, C. Xiao, S. Fan, J. Liu, W. Zhang, W. Xu, W. Tong, J. Liao, Y. Zhou, B. Ye, Y. Xie, Vacancy associates-rich ultrathin nanosheets for high performance and flexible nonvolatile memory device, *J. Am. Chem. Soc.* 137 (2015) 3102–3108, doi:[10.1021/jacs.5b00021](https://doi.org/10.1021/jacs.5b00021).
- [5] L. Zhang, S. Li, M.A. Squillaci, X. Zhong, Y. Yao, E. Orgiu, P. Samorì, Supramolecular self-assembly in a sub-micrometer electrocyclic cavity: fabrication of heat-reversible π -gel memristor, *J. Am. Chem. Soc.* 139 (2017) 14406–14411, doi:[10.1021/jacs.7b04347](https://doi.org/10.1021/jacs.7b04347).
- [6] B. Mohammad, M.A. Jaoude, V. Kumar, D.M. Al Homouz, H.A. Nahla, M. Al-Qutayri, N. Christoforou, State of the art of metal oxide memristor devices, *Nanotechnol. Rev.* 5 (2016) 311–329, doi:[10.1515/ntrev-2015-0029](https://doi.org/10.1515/ntrev-2015-0029).
- [7] M.A. Zidan, J.P. Strachan, W.D. Lu, The future of electronics based on memristive systems, *Nat. Electron.* 1 (2018) 22–29, doi:[10.1038/s41928-017-0006-8](https://doi.org/10.1038/s41928-017-0006-8).
- [8] T. Fu, X. Liu, H. Gao, J.E. Ward, X. Liu, B. Yin, Z. Wang, Y. Zhuo, D.J.F. Walker, J. Joshua Yang, J. Chen, D.R. Lovley, J. Yao, Bioinspired bio-voltage memristors, *Nat. Commun.* 11 (2020) 1–10, doi:[10.1038/s41467-020-15759-y](https://doi.org/10.1038/s41467-020-15759-y).
- [9] D. Ielmini, Resistive switching memories based on metal oxides: mechanisms, reliability and scaling, *Semicond. Sci. Technol.* 31 (2016) 1–25, doi:[10.1088/0268-1242/31/6/063002](https://doi.org/10.1088/0268-1242/31/6/063002).
- [10] J. Borghetti, G.S. Snider, P.J. Kuekes, J.J. Yang, D.R. Stewart, R.S. Williams, Memristive switches enable stateful logic operations via material implication, *Nature* 464 (2010) 873–876, doi:[10.1038/nature08940](https://doi.org/10.1038/nature08940).
- [11] T. Prodromakis, C. Toumazou, A review on memristive devices and applications, in: *Proceedings of the IEEE International Conference on Electronics, Circuits and Systems (ICECS)*, 2010, pp. 934–937, doi:[10.1109/ICECS.2010.5724666](https://doi.org/10.1109/ICECS.2010.5724666).
- [12] R. Waser, M. Aono, Nanoionics-based resistive switching memories, *Nanosci. Technol.* (2009) 158–165 *A Collect. Rev. from Nat. Journals.*, doi:[10.1142/9789814287005_0016](https://doi.org/10.1142/9789814287005_0016).
- [13] K. Miller, K.S. Nalwa, A. Bergerud, N.M. Neihart, S. Chaudhary, Memristive behavior in thin anodic Titania, *IEEE Electron Device Lett.* 31 (2010) 737–739, doi:[10.1109/LED.2010.2049092](https://doi.org/10.1109/LED.2010.2049092).
- [14] I.B. Dorosheva, A.S. Vokhmintsev, R.V. Kamalov, A.O. Gryaznov, I.A. Weinstein, Oxide layer thickness effects on the resistance switching characteristics of Ti/TiO₂-NT/Au structure, in: *Proceedings of the 2018 Ural Symposium on Biomedical Engineering, Radioelectronics and Information Technology (US-BERET)*, 2018, pp. 279–282, doi:[10.1109/USBERET.2018.8384604](https://doi.org/10.1109/USBERET.2018.8384604).
- [15] M.V. Diamanti, R. Pisoni, A. Cologni, A. Brenna, F. Corinto, M.P. Pedeferri, Anodic oxidation as a means to produce memristive films, *J. Appl. Biomater. Funct. Mater.* 14 (2016) e290–e295, doi:[10.5301/jabfm.5000290](https://doi.org/10.5301/jabfm.5000290).
- [16] J. Lu, Y. Kuo, J.Y. Tewg, Hafnium-doped tantalum oxide high-k gate dielectrics, *J. Electrochem. Soc.* 153 (2006) G410, doi:[10.1149/1.2180647](https://doi.org/10.1149/1.2180647).
- [17] J. Lu, Y. Kuo, Hafnium-doped tantalum oxide high-k dielectrics with sub-2nm equivalent oxide thickness, *Appl. Phys. Lett.* 87 (2005) 1–3, doi:[10.1063/1.2140482](https://doi.org/10.1063/1.2140482).
- [18] I. Zrinski, C.C. Mardare, L.I. Jinga, J.P. Kollender, G. Socol, A.W. Hassel, A.I. Mardare, Phosphate incorporation in anodic hafnium oxide memristors, *Appl. Surf. Sci.* 548 (2021) 149093, doi:[10.1016/j.apsusc.2021.149093](https://doi.org/10.1016/j.apsusc.2021.149093).
- [19] A. Zaffora, F. Di Quarto, H. Habazaki, I. Valov, M. Santamaria, Electrochemically prepared oxides for resistive switching memories, *Faraday Discuss.* 213 (2019) 165–181, doi:[10.1039/c8fd000112j](https://doi.org/10.1039/c8fd000112j).
- [20] S. Dueñas, E. Castán, J. Barbolla, R.R. Kola, P.A. Sullivan, Use of anodic tantalum pentoxide for high-density capacitor fabrication, *J. Mater. Sci. Mater. Electron.* 10 (1999) 379–384, doi:[10.1023/a:1008901624514](https://doi.org/10.1023/a:1008901624514).
- [21] T. Dobashi, T. Umezawa, K. Sasaki, A. Noya, The oxidation process and dissipation factor of Al/Ta/Hf multilayered anodized thin-film capacitors, *Electron. Commun. Jpn. Part II Electron.* 77 (1994) 59–66, doi:[10.1002/ecjb.4420771207](https://doi.org/10.1002/ecjb.4420771207).
- [22] A.I. Mardare, A. Ludwig, A. Savaş, A.D. Wiecek, A.W. Hassel, Combinatorial investigation of Hf-Ta thin films and their anodic oxides, *Electrochim. Acta* 55 (2010) 7884–7891, doi:[10.1016/j.electacta.2010.03.066](https://doi.org/10.1016/j.electacta.2010.03.066).
- [23] M.M. Lohrengel, *Rev. J. Mater. Sci.* 12 (1993) 243–294, doi:[10.1016/0927-796X\(94\)90011-6](https://doi.org/10.1016/0927-796X(94)90011-6).
- [24] J.U. Woo, H.G. Hwang, S.M. Park, T.G. Lee, S. Nahm, Improvement in conductance modulation linearity of artificial synapses based on NaNbO₃ memristor, *Appl. Mater. Today* 19 (2020) 100582, doi:[10.1016/j.apmt.2020.100582](https://doi.org/10.1016/j.apmt.2020.100582).
- [25] S. Choi, S. Jang, J.H. Moon, J.C. Kim, H.Y. Jeong, P. Jang, K.J. Lee, G. Wang, A self-rectifying TaO_y/nanoporous TaO_x memristor synaptic array for learning and energy-efficient neuromorphic systems, *NPG Asia Mater.* 10 (2018) 1097–1106, doi:[10.1038/s41427-018-0101-y](https://doi.org/10.1038/s41427-018-0101-y).
- [26] M. Sophocleous, N. Mohammadian, L.A. Majewski, J. Georgiou, Solution-processed, low voltage tantalum-based memristive switches, *Mater. Lett.* 269 (2020) 127676, doi:[10.1016/j.matlet.2020.127676](https://doi.org/10.1016/j.matlet.2020.127676).
- [27] I. Zrinski, A. Minenkov, C.C. Mardare, J.P. Kollender, S.A. Lone, A.W. Hassel, A.I. Mardare, Influence of electrolyte selection on performance of tantalum anodic oxide memristors, *Appl. Surf. Sci.* 565 (2021) 150608, doi:[10.1016/j.apsusc.2021.150608](https://doi.org/10.1016/j.apsusc.2021.150608).
- [28] I. Zrinski, C.C. Mardare, L.I. Jinga, J.P. Kollender, G. Socol, A. Minenkov, A.W. Hassel, A.I. Mardare, Electrolyte-dependent modification of resistive switching in anodic hafnia, *Nanomaterials* 11 (2021) 1–18, doi:[10.3390/nano11030666](https://doi.org/10.3390/nano11030666).
- [29] S. Ravandi, A. Minenkov, C.C. Mardare, J.P. Kollender, H. Groiss, A.W. Hassel, A.I. Mardare, Gallium-enhanced aluminum and copper electromigration performance for flexible electronics, *ACS Appl. Mater. Interfaces* 13 (2021) 6960–6974, doi:[10.1021/acsami.0c22211](https://doi.org/10.1021/acsami.0c22211).
- [30] Sodium phosphate, Cold Spring Harb. Protoc. 2006 (2006) pdb.rec8303, doi:[10.1101/pdb.rec8303](https://doi.org/10.1101/pdb.rec8303).
- [31] S. Tanuma, C.J. Powell, D.R. Penn, Proposed formula for electron inelastic mean free paths based on calculations for 31 materials, *Surf. Sci.* 192 (1987) L849–L857, doi:[10.1016/S0039-6028\(87\)81156-1](https://doi.org/10.1016/S0039-6028(87)81156-1).
- [32] D.S. Jeong, H. Schroeder, R. Waser, Coexistence of bipolar and unipolar resistive switching behaviors in a Pt TiO₂ Pt stack, *Electrochem. Solid State Lett.* 10 (2007) 1–4, doi:[10.1149/1.2742989](https://doi.org/10.1149/1.2742989).
- [33] M. Lanza, H.S.P. Wong, E. Pop, D. Ielmini, D. Strukov, B.C. Regan, L. Larcher, M.A. Villena, J.J. Yang, L. Goux, A. Belmonte, Y. Yang, F.M. Puglisi, J. Kang, B. Magyari-Köpe, E. Yalon, A. Kenyon, M. Buckwell, A. Mehonic, A. Shluger, H. Li, T.H. Hou, B. Hudec, D. Akinwande, R. Ge, S. Ambrogio, J.B. Roldan, E. Miranda, J. Suñe, K.L. Pey, X. Wu, N. Raghavan, E. Wu, W.D. Lu, G. Navarro, W. Zhang, H. Wu, R. Li, A. Holleitner, U. Wurstbauer, M.C. Lemme, M. Liu, S. Long, Q. Liu, H. Lv, A. Padovani, P. Pavan, I. Valov, X. Jing, T. Han, K. Zhu, S. Chen, F. Hui, Y. Shi, Recommended methods to study resistive switching devices, *Adv. Electron. Mater.* 5 (2019) 1–28, doi:[10.1002/aeml.201800143](https://doi.org/10.1002/aeml.201800143).
- [34] H. Abbas, Y. Abbas, G. Hassan, A.S. Sokolov, Y.R. Jeon, B. Ku, C.J. Kang, C. Choi, The coexistence of threshold and memory switching characteristics of ALD HfO₂memristor synaptic arrays for energy-efficient neuromorphic computing, *Nanoscale* 12 (2020) 14120–14134, doi:[10.1039/d0nr02335c](https://doi.org/10.1039/d0nr02335c).
- [35] B. Song, R. Cao, H. Xu, S. Liu, H. Liu, Q. Li, A HfO₂ /site based dual-layer selector device with minor threshold voltage variation, *Nanomaterials* 9 (2019), doi:[10.3390/nano9030408](https://doi.org/10.3390/nano9030408).
- [36] L. Shi, G. Zheng, B. Tian, B. Dkhil, C. Duan, Research progress on solutions to the sneak path issue in memristor crossbar arrays, *Nanoscale Adv.* 2 (2020) 1811–1827, doi:[10.1039/d0na00100g](https://doi.org/10.1039/d0na00100g).
- [37] H. Abbas, A. Ali, J. Jung, Q. Hu, M.R. Park, H.H. Lee, T.S. Yoon, C.J. Kang, Reversible transition of volatile to non-volatile resistive switching and compliance current-dependent multistate switching in IGZO/MnO RRAM devices, *Appl. Phys. Lett.* 114 (2019), doi:[10.1063/1.5082901](https://doi.org/10.1063/1.5082901).
- [38] G. Du, H. Li, Q. Mao, Z. Ji, Controllable volatile to nonvolatile resistive switching conversion and conductive filaments engineering in Cu/ZrO₂/Pt devices, *J. Phys. D Appl. Phys.* (2016) 49, doi:[10.1088/0022-3727/49/44/445105](https://doi.org/10.1088/0022-3727/49/44/445105).

- [39] Y. Li, P. Yuan, L. Fu, R. Li, X. Gao, C. Tao, Coexistence of diode-like volatile and multilevel nonvolatile resistive switching in a $\text{ZrO}_2/\text{TiO}_2$ stack structure, *Nanotechnology* (2015) 26, doi:[10.1088/0957-4484/26/39/391001](https://doi.org/10.1088/0957-4484/26/39/391001).
- [40] A.A. Minnekhanov, A.V. Emelyanov, D.A. Lapkin, K.E. Nikiruy, B.S. Shvetsov, A.A. Nesmelov, V.V. Rylkov, V.A. Demin, V.V. Erokhin, Parylene based memristive devices with multilevel resistive switching for neuromorphic applications, *Sci. Rep.* 9 (2019) 1–9, doi:[10.1038/s41598-019-47263-9](https://doi.org/10.1038/s41598-019-47263-9).
- [41] P. Rabbani, R. Dehghani, N. Shahpari, A multilevel memristor-CMOS memory cell as a ReRAM, *Microelectron. J.* 46 (2015) 1283–1290, doi:[10.1016/j.mejo.2015.10.006](https://doi.org/10.1016/j.mejo.2015.10.006).
- [42] U. Russo, D. Kamalanathan, D. Ielmini, A.L. Lacaita, M.N. Kozicki, Study of multilevel programming in programmable metallization cell (PMC) memory, *IEEE Trans. Electron Devices* 56 (2009) 1040–1047, doi:[10.1109/TED.2009.2016019](https://doi.org/10.1109/TED.2009.2016019).
- [43] L. Goux, S. Spiga, Unipolar resistive-switching mechanisms, in: *Resistive Switching*, 2016, pp. 363–394, doi:[10.1002/9783527680870.ch13](https://doi.org/10.1002/9783527680870.ch13).
- [44] M. Zhang, S. Long, Y. Li, Q. Liu, H. Lv, E. Miranda, J. Suñé, M. Liu, Analysis on the filament structure evolution in reset transition of $\text{Cu}/\text{HfO}_2/\text{Pt}$ RRAM device, *Nanoscale Res. Lett.* (2016) 11, doi:[10.1186/s11671-016-1484-8](https://doi.org/10.1186/s11671-016-1484-8).
- [45] M.J. Wang, S. Gao, F. Zeng, C. Song, F. Pan, Unipolar resistive switching with forming-free and self-rectifying effects in $\text{Cu}/\text{HfO}_2/\text{n-Si}$ devices, *AIP Adv.* 6 (2016), doi:[10.1063/1.4941839](https://doi.org/10.1063/1.4941839).
- [46] L. Wu, H. Liu, J. Li, S. Wang, X. Wang, A multi-level memristor based on Al-doped HfO_2 thin film, *Nanoscale Res. Lett.* 14 (2019), doi:[10.1186/s11671-019-3015-x](https://doi.org/10.1186/s11671-019-3015-x).
- [47] G.S. Kim, T.H. Park, H.J. Kim, T.J. Ha, W.Y. Park, S.G. Kim, C.S. Hwang, Investigation of the retention performance of an ultra-thin HfO_2 resistance switching layer in an integrated memory device, *J. Appl. Phys.* (2018) 124, doi:[10.1063/1.5033967](https://doi.org/10.1063/1.5033967).
- [48] S. Dirkmann, J. Kaiser, C. Wenger, T. Mussenbrock, Filament growth and resistive switching in hafnium oxide memristive devices, *ACS Appl. Mater. Interfaces* 10 (2018) 14857–14868, doi:[10.1021/acsami.7b19836](https://doi.org/10.1021/acsami.7b19836).
- [49] S. Siol, J. Mann, J. Newman, T. Miyayama, K. Watanabe, P. Schmutz, C. Cancellieri, L.P.H. Jeurgens, Concepts for chemical state analysis at constant probing depth by lab-based XPS/HAXPES combining soft and hard X-ray sources, *Surf. Interface Anal.* 52 (2020) 802–810, doi:[10.1002/sia.6790](https://doi.org/10.1002/sia.6790).
- [50] C.D. Wagner, Chemical shifts of Auger lines, and the Auger parameter, *Faraday Discuss. Chem. Soc.* 60 (1975) 291–300, doi:[10.1039/DC9756000291](https://doi.org/10.1039/DC9756000291).
- [51] J.A. Wagner, C.D. Passoja, D.E. Hillery, H.F. Kinisky, T.G. Six, H.A. Jansen, W.T. Taylor, Auger and photoelectron line energy relationships in aluminium-oxygen and silicon-oxygen compounds, *J. Vac. Sci. Technol.* 21 (1982) 933, doi:[10.1016/0042-207x\(85\)90575-5](https://doi.org/10.1016/0042-207x(85)90575-5).
- [52] C.D. Wagner, A. Joshi, The auger parameter, its utility and advantages: a review, *J. Electron Spectros. Relat. Phenom.* 47 (1988) 283–313, doi:[10.1016/0368-2048\(88\)85018-7](https://doi.org/10.1016/0368-2048(88)85018-7).
- [53] P. Weightman, Auger spectroscopy and the electronic structure of crystals, *J. Electron Spectros. Relat. Phenom.* 68 (1994) 127–138, doi:[10.1016/0368-2048\(94\)02109-0](https://doi.org/10.1016/0368-2048(94)02109-0).
- [54] J.F. Watts, J. Wolstenholme, *An Introduction to Surface Analysis by XPS and AES*, 2019, doi:[10.1002/9781119417651](https://doi.org/10.1002/9781119417651).
- [55] G. Moretti, Auger parameter and wagner plot in the characterization of chemical states: initial and final state effects, *J. Electron Spectros. Relat. Phenom.* 76 (1995) 365–370, doi:[10.1016/0368-2048\(95\)02443-3](https://doi.org/10.1016/0368-2048(95)02443-3).
- [56] K. Weller, Z. Wang, L.P.H. Jeurgens, E.J. Mittemeijer, Thermodynamics controls amorphous oxide formation: exclusive formation of a stoichiometric amorphous ($\text{Al}_{0.33}\text{Zr}_{0.67}$) $\text{O}_{1.83}$ phase upon thermal oxidation of Al-Zr, *Acta Mater.* 94 (2015) 134–142, doi:[10.1016/j.actamat.2015.04.038](https://doi.org/10.1016/j.actamat.2015.04.038).
- [57] C.B. Williams, D.B. Carter, *Transmission Electron Microscopy*, 2009, doi:[10.1007/978-0-387-76501-3](https://doi.org/10.1007/978-0-387-76501-3).
- [58] K. Persson, Materials data on Pt (SG:225) by materials project, (2015), doi:[10.17188/1189002](https://doi.org/10.17188/1189002).
- [59] K. Persson, Materials data on HfO_2 (SG:225) by materials project, (2014), doi:[10.17188/1267443](https://doi.org/10.17188/1267443).
- [60] K. Persson, Materials data on HfO_2 (SG:14) by materials project, (2014), doi:[10.17188/1206948](https://doi.org/10.17188/1206948).
- [61] J. Wang, L. Li, H. Huan, X. Pan, S.S. Nonnenmann, Highly uniform resistive switching in HfO_2 films embedded with ordered metal nanodot arrays, *Adv. Funct. Mater.* 29 (2019) 1–11, doi:[10.1002/adfm.201808430](https://doi.org/10.1002/adfm.201808430).
- [62] L. Gao, Y. Li, Q. Li, Z. Song, F. Ma, Enhanced resistive switching characteristics in Al_2O_3 memory devices by embedded Ag nanoparticles, *Nanotechnology* (2017) 28, doi:[10.1088/1361-6528/aa6cd0](https://doi.org/10.1088/1361-6528/aa6cd0).